Magnetization-induced second- and third-harmonic generation in magnetophotonic crystals

Oleg A. Aktsipetrov, Tatyana V. Dolgova, Andrey A. Fedyanin, and Tatyana V. Murzina

Department of Physics, Moscow State University, 119992 Moscow, Russia

Mitsuteru Inoue, Kazuhiro Nishimura, and Hironaga Uchida

Toyohashi University of Technology, 441-8580 Toyohashi, Japan

Received April 29, 2004; revised manuscript received September 2, 2004; accepted September 20, 2004

The results of our recent studies of magnetization-induced nonlinear-optical second- and third-order effects in magnetophotonic crystals and magnetophotonic microcavities are surveyed. Magnetophotonic crystals (MPCs) are fabricated from a stack of four repetitions of λ/4-thick layers of Bi-substituted yttrium iron garnet (Bi:YIG) and λ/4-thick SiO_2 layers. Magnetophotonic microcavities (MMCs) are formed from two dielectric (nonmagnetic) Bragg reflectors and ferromagnetic cavity spacers that are λ/2-thick Bi:YIG layers. The nonlinear magneto-optical Kerr effect (NOMOKE), both in magnetization-induced second-harmonic generation (MSHG) and magnetization-induced third-harmonic generation (MTHG), is observed in MMCs at wavelengths of the resonant microcavity modes. Magnetization-induced variations of MSHG and MTHG intensities, as well as magnetization-induced shift of phase and rotation of polarization of second and third-harmonic waves, are observed in proper—transversal, longitudinal, or polar—NOMOKE configurations. Manyfold enhancement of the absolute values of both the MSHG and MTHG intensities are attributed to the localization of the resonant fundamental radiation in Bi:YIG microcavity spacers. The NOMOKE in MSHG intensity is observed in MPCs in the spectral range of photonic bandgap (PBG) edges. The MSHG intensity reveals enhancement by a factor of more than 10^2 if the fundamental wavelength is tuned in the vicinity of the PBG edge. This enhancement is attributed to the fulfillment of the phase-matching conditions for MSHG effect in layered structures with periodic modulation of both optical (magneto-optical) and nonlinear optical parameters.

OCIS codes: 160.4330, 160.3820, 190.4350, 300.6420.

1. INTRODUCTION

The studies of nonlinear magneto-optical effects in magnetophotonic crystals (MPCs) are twofold motivated, as both photonic bandgap (PBG) materials and nonlinear magneto-optics have each attracted considerable attention recently. The PBG structures—photonic crystals (PCs) and microcavities (MCs)—have been the subject of intensive studies for the past ten years.[1] Quick progress in fabrication techniques of the PBG materials brought about the observation of new phenomena in contemporary optics related to the propagation of light through sophisticated artificial structures. One of the potential advantages of PBG materials is significant enhancement of nonlinear optical effects such as second-harmonic (SHG) and third-harmonic (THG) generation in PCs. For example, modification of the dispersion law of electromagnetic waves near the PBG edges allows one to fulfill effectively the phase-matching conditions for SHG as the fundamental or second-harmonic (SH) wave is tuned near the PBG edge.[2] The SHG enhancement in one-dimensional photonic crystals due to phase-matching was proposed in Ref. 3 and later was observed in PCs formed from different semiconductors and dielectrics.[4–7] Another mechanism of SHG and THG enhancement is realized in MCs possessing the resonant MC mode located in the PBG. The fundamental field is strongly localized in the MC spacer if the wavelength of the fundamental wave is adjusted to the resonant MC mode. This brings about the enhancement of nonlinear optical response that has been recently observed in MCs with chromophore,[8] polymeric,[9] or semiconductor[10,11] spacers.

A new domain of nonlinear optics appears as the second- and third-order structural nonlinearities are combined with the broken time-reversal symmetry that is due to the magnetization of ferromagnetic materials. As a result of this combination, SHG and THG become very sensitive to control by external magnetic impacts. Experimental studies of magnetization-induced second-harmonic generation (MSHG) may be traced back to the late 1980s as the nonlinear magneto-optical Kerr effect (NOMOKE) and nonlinear Faraday effect in MSHG were observed in thin, magnetic garnet films.[12,13] Later MSHG was observed in a broad variety of magnetic materials and structures such as atomically clean surfaces of magnetic single crystals under ultrahigh-vacuum conditions[14] or in air,[15] in planar-layered magnetic structures,[16–19] epitaxial magnetic garnet films,[20–22] and nanogranular films.[23,24] Giant NOMOKE, which was observed in granular films, demonstrated the role of local optical field enhancement in composite magnetic materials as a result of assistance of MSHG by resonant excitation of local plasmons in metallic nanoparticles. Another class of composite magnetic materials in which the close mechanism of NOMOKE enhancement is expected are

magnetic PBG materials. This idea initiated nonlinear magneto-optical studies in MPCs, and MSHG[25,26] and MTHG[27] have been observed recently. Diffraction in MSHG from periodic arrays of magnetic stripes, which can be considered MPCs in a certain sense, has also been observed.[28]

Generally, various magnetic PBG materials (for a brief review see Ref. 29) yield a mechanism for molding the flow of light that is flexible under external control impacts such as dc magnetic fields. For this reason they can find widespread use as optical isolators, optical switchers, magnetic field sensors, and spatial light modulators, as well as new materials for magneto-optical imaging and detection. MPCs with the single magnetic layer squeezed between two high-finesse dielectric Bragg reflectors have been designed recently.[30] Such MPCs act as microcavities and have a resonant optical transition–microcavity mode located in the PBG. Spatial localization of the optical field at the wavelength resonant with the microcavity mode leads to the Faraday-effect enhancement observed in MPCs with magnetic, Bi-substituted yttrium iron garnet (Bi:YIG),[30] Co-ferrite,[31] or Co-Sm-O granular film[32] spacers. More advanced MPCs formed of multilayer stacks of $\lambda/4$-thick-Bi:YIG–$\lambda/4$-thick-SiO_2 pairs that were developed recently[33] show prospective magneto-optical and nonlinear magneto-optical properties.

In this paper, recently published[27,34,35] and new results of nonlinear magneto-optical studies, both in Bi:YIG-based MPCs and magnetophotonic microcavities (MMCs), are surveyed. The mechanisms of magnetization-induced variations in SHG and THG intensity, magnetization-induced rotations of the SH and TH wave polarization, and relative SH phase shifts are discussed in terms of local field enhancement in MMCs and phase-matching fulfillment in MPCs.

The paper is organized as follows. Section 2 presents a brief phenomenological description of MSHG and MTHG in magnetic films and analysis of symmetry properties of the quadratic and cubic susceptibility tensors of Bi:YIG layers of MPCs and MMCs. The details of MPC and MMC sample fabrication and the experimental setup are given in Section 3. Section 4 is devoted to the observation of the NOMOKE in MSHG and MTHG for MPCs and MMCs. The studies are concluded in Section 5.

2. BACKGROUND

In centrosymmetric materials the magnetization vector does not break inversion symmetry because of its axial nature. Consideration of the nonlinear magnet-optical effects in SHG within the electric-dipole approximation requires the lack of inversion symmetry. Magnetization-induced effects in THG can be observed in materials of any symmetry. Electromagnetic fields at the doubled and tripled frequencies of the fundamental radiation are induced by the quadratic and cubic nonlinear polarizations $\mathbf{P}^{(2)}(2\omega)$ and $\mathbf{P}^{(3)}(3\omega)$ that are written in the electric-dipole approximation as

$$\mathbf{P}^{(2)}(2\omega) = \chi^{(2)}(\mathbf{M}):\mathbf{E}_\omega\mathbf{E}_\omega, \tag{1}$$

$$\mathbf{P}^{(3)}(3\omega) = \chi^{(3)}(\mathbf{M}):\mathbf{E}_\omega\mathbf{E}_\omega\mathbf{E}_\omega. \tag{2}$$

$\mathbf{E}_\omega$ is the fundamental field amplitude and $\chi^{(2)}$ and $\chi^{(3)}$ are the quadratic and cubic electric-dipole susceptibility tensors of magnetic material (garnets) forming the MPCs and MMCs. Hereafter, the influence of the domain walls is neglected since all effects in MSHG and MTHG presented here are observed under saturating dc magnetic fields provided for the single-domain state of magnetic garnet films. Dependence of the $\chi^{(2)}$ and $\chi^{(3)}$ tensors on the magnetization vector $\mathbf{M}$ is written as a sum of three terms:

$$\chi^{(2)}(\mathbf{M}) = \chi^{(2,0)} + \chi^{(2,1)} \cdot \mathbf{M} + \chi^{(2,2)}:\mathbf{MM}, \tag{3}$$

$$\chi^{(3)}(\mathbf{M}) = \chi^{(3,0)} + \chi^{(3,1)} \cdot \mathbf{M} + \chi^{(3,2)}:\mathbf{MM}. \tag{4}$$

Tensors $\chi^{(2,0)}$ and $\chi^{(3,0)}$ describe the nonmagnetic (crystallographic) contributions to $\chi^{(2)}$ and $\chi^{(3)}$, respectively; axial tensors (or pseudotensors) $\chi^{(2,1)}$ and $\chi^{(3,1)}$ induce the MSHG and MTHG contributions in $\mathbf{P}^{(2)}(2\omega)$ and $\mathbf{P}^{(3)} \times (3\omega)$, which are odd in the magnetization; while the tensors $\chi^{(2,2)}$ and $\chi^{(3,2)}$ are responsible for the MSHG and MTHG terms even in $\mathbf{M}$. Nonzero tensor elements can be found through invariance of susceptibility tensors under symmetry elements of the point group of the particular material considered, taking into account different transformation matrices for polar and axial frames.

Crystals of yttrium iron garnets possess inversion symmetry; however, thin garnet films, both epitaxial and polycrystalline, are noncentrosymmetric. The lowering of symmetry of the initially centrosymmetric garnet lattice was deduced by observation of a magnetoelectrical effect linear in the electric field that requires a medium with broken inversion symmetry.[36] Lattice deformation and variation of the lattice parameters of polycrystalline yttrium garnet films due to the formation of oxygen vacancies is obtained directly from x-ray-diffraction analysis.[37] Numerous SHG studies in magnetic garnet films also prove the breaking of inversion symmetry. For example, enhancement of quadratic susceptibility of Bi:YIG films in comparison with undoped YIG film was directly observed in reflected[38] and transmitted[22] SHG. Temperature variations of the SHG response were observed in Bi-doped garnet films grown on gadolinium gallium garnet substrates.[20,39] Thickness dependence of SH intensity from Bi:YIG films is reported in Ref. 12.

Inversion symmetry of Bi:YIG films is broken since the film plane is not a mirror plane any longer. Such growth-induced film anisotropy is most likely attributed to local distortion of the garnet cell by bismuth atoms and their ordering on the nonequivalent crystallographic sites during film growth.[39] Another source of enhanced quadratic susceptibility of Bi:YIG films has been proposed as lattice misfit strain in the deformed garnet layer near the substrate[37,40] forming the polar axis along the film normal. Both mechanisms could be responsible for the breaking of inversion symmetry in the Bi:YIG layers in the MPCs and MMCs studied. The garnet films used are heavily doped by Bi atoms (one Bi atom for two Y atoms), thus large distortions in the dodecahedral, rare-earth-ion sublattice of the garnet crystal cell are expected. The polar axis along the Bi:YIG film normal can also be produced by film sputtering on the fused quartz substrate or amorphous silicon dioxide layers and subsequent high-

temperature annealing of the Bi:YIG layer with two nonequivalent—garnet–air and garnet–silicon dioxide—interfaces.

However, a description of microscopic mechanisms of inversion-symmetry breaking in Bi:YIG films remains incomplete. We use the macroscopic description of electric-dipole SHG sources in garnet films, which deals with appropriate symmetry elements related to the whole garnet film. Bi:YIG films are treated as layers possessing the ∞m symmetry group with mirror planes perpendicular to the film plane. Take a Cartesian frame $\mathbf{e}_x$, $\mathbf{e}_y$, $\mathbf{e}_z$ with the xy plane perpendicular to the symmetry planes m_z. The xy plane is a film surface and the xz plane denotes the plane of incidence. The nonzero elements of the $\chi^{(2,1)}$ and $\chi^{(3,1)}$ tensors describing the magnetization-induced quadratic and cubic polarizations $P_i^{(2),M} = \chi_{ijkL}^{(2,1)} E_j^{\omega} E_k^{\omega} M_L$ and $P_i^{(3),M} = \chi_{ijklN}^{(3,1)} E_j^{\omega} E_k^{\omega} E_l^{\omega} M_N$ are shown in Table 1. For comparison the nonzero elements of the $\chi^{(2,0)}$ and $\chi^{(3,0)}$ tensors defining the nonmagnetic component of the quadratic and cubic polarizations $P_i^{(2),NM} = \chi_{ijk}^{(2,0)} E_j^{\omega} E_k^{\omega}$ and $P_i^{(3),NM} = \chi_{ijkl}^{(3,0)} E_j^{\omega} E_k^{\omega} E_l^{\omega}$ are also shown. Tensor elements are divided into the magnetization directions and polarization combinations to which they contribute.

In transparent materials elements of the $\chi^{(2,0)}$ and $\chi^{(3,0)}$ tensors are real values, but components of $\chi^{(2,1)}$ and $\chi^{(3,1)}$ tensors are imaginary values. Interference between nonmagnetic and magnetization-induced components of SH or TH fields, which leads to observation of magnetization-induced effects in the SH and TH intensities odd in the magnetization, requires absorption. This is the case for Bi:YIG films that have an absorption band above 550–500 nm, depending on the Bi content.[41] Bi:YIG film transparency in the red and IR regions allows the high-contrast, multiple interference of the fundamental radiation that results in pronounced PBG effects and localization of the fundamental field resonant with the microcavity mode.

3. SAMPLES AND SETUP

MMCs are formed from two dielectric Bragg reflectors and a ferromagnetic cavity spacer. The reflectors consist of five pairs of alternating quarter-wavelength-thick SiO_2 and Ta_2O_5 layers. The cavity spacer is a Bi:YIG layer $Bi_{1.0}Y_{2.0}Fe_5O_x$. The spacer optical thickness is a half wavelength. MMCs are grown on a glass substrate by the rf sputtering of corresponding targets in an Ar^+ atmosphere with sputtering pressure of 6 mTorr. Before fabrication of the top Bragg reflector the sample is annealed in air at 700 °C for 20 min for residual oxidation and crystallization of the Bi:YIG spacer. The MMC samples have $\lambda_{MC} \approx 900$ nm and $\lambda_{MC} \approx 1115$ nm that correspond to Bi:YIG spacer thicknesses of ≈195 nm and 245 nm, respectively. Hereafter λ_{MC} denotes the spectral position of the microcavity mode at normal incidence and is determined by the optical thickness of the layers forming the MMCs.

For MPCs λ_{MC} is replaced by λ_{PC}, which is related to the PBG center of the MPC at normal incidence. MPCs are fabricated from a stack of four repetitions of $3\lambda_{PC}$/4-thick Bi:YIG layers and λ_{PC}/4-thick SiO_2 layers with $\lambda_{PC} \approx 950$ nm.[33] Topmost and bottommost layers of the MPCs are Bi:YIG. MPCs are grown on a fused quartz substrate by rf sputtering. After evaporation of each successive Bi:YIG layer, the sample is removed from the sputtering chamber and annealed in air at 700 °C. Cleavages of MMCs and MPCs are studied with a field-emission-scanning-electron microscope (FESEM). FESEM images are shown in Fig. 1. Good reflector periodicity and sharp interfaces between magnetic garnet and dielectric layers are seen. Small, gradual increase of the upper garnet layer thicknesses in MPCs is apparently associated with different shrinkage of the garnet films during annealing and changes in sputtering rate due to the change in substrate temperature during sputtering. Hysteresis loops measured in a vibrating-sample magnetometer show that the coercivity of MPCs and MMCs is approximately 30 Oe for tangential field application. A saturating field that is slightly above 100 Oe indicates the easy-magnetization axis aligned along the Bi:YIG surfaces.

Spectroscopy of microcavities and one-dimensional photonic crystals implies tuning of the wave-vector component k_z parallel to the periodicity direction. Two configu-

Table 1. Nonzero Elements of $\chi_{ijkL}^{(2,1)}$, $\chi_{ijkN}^{(3,1)}$, $\chi_{ijk}^{(2,0)}$, and $\chi_{ijkl}^{(3,0)}$ Tensors for the ∞m Symmetry Group Divided into the Magnetization Vector Components (Columns) and Polarization Combinations of the Fundamental and Harmonic Waves (Rows)

	Third-Harmonic Generation				Second-Harmonic Generation			
	$\times M_X$[a]	$\times M_Y$	$\times M_Z$	$\times 1$	$\times M_X$	$\times M_Y$	$\times M_Z$	$\times 1$
$s \rightarrow s$	0	0	0	χ_{yyyy}	χ_{yyyX}	0	0	0
$s \rightarrow p$	χ_{zyyyX}	0	χ_{xyyyZ}	0	0	χ_{xyyY}	0	χ_{zyy}
$p \rightarrow s$	χ_{yxxzX}, χ_{yzzzX}	0	χ_{yxzzZ}, χ_{yxxxZ}	0	χ_{yxxX}, χ_{yzzX}	0	χ_{yxzZ}	0
$p \rightarrow p$	0	χ_{zxzzY}, χ_{xxxzY}, χ_{zxxxY}, χ_{xzzzY}	0	χ_{zzzz}, χ_{xxxx}, χ_{zxxz}, χ_{xxzz}	0	χ_{xxxY}, χ_{xzzY}, χ_{zxzY}	0	χ_{zzz}, χ_{xzx}, χ_{zxx}
$m \rightarrow s$	χ_{yyyzX}	χ_{yxyzY}	χ_{yxyyZ}	χ_{yxxy}, χ_{yyzz}	0	χ_{yxyY}	0	χ_{yzy}
$m \rightarrow p$	χ_{zxxyX}, χ_{xyzzX}, χ_{xxyzX}	χ_{zxyyY}, χ_{xyyzY}	χ_{xyzzZ}, χ_{xxxyZ}	χ_{xxyy}, χ_{zyyz}	χ_{zyzX}, χ_{xyyX}	0	χ_{xyzZ}	0

[a] M_X, M_Y, and M_Z relate to the longitudinal, transversal, and polar NOMOKE configurations. Columns containing nonmagnetic SHG and THG contributions are denoted by $\times 1$. m indicates the mixed polarization of the fundamental radiation, which is 45°-rotated relative to the s and p polarizations. The bottom two rows contain the nonzero tensor elements that contribute in polarization combinations with m polarization only.

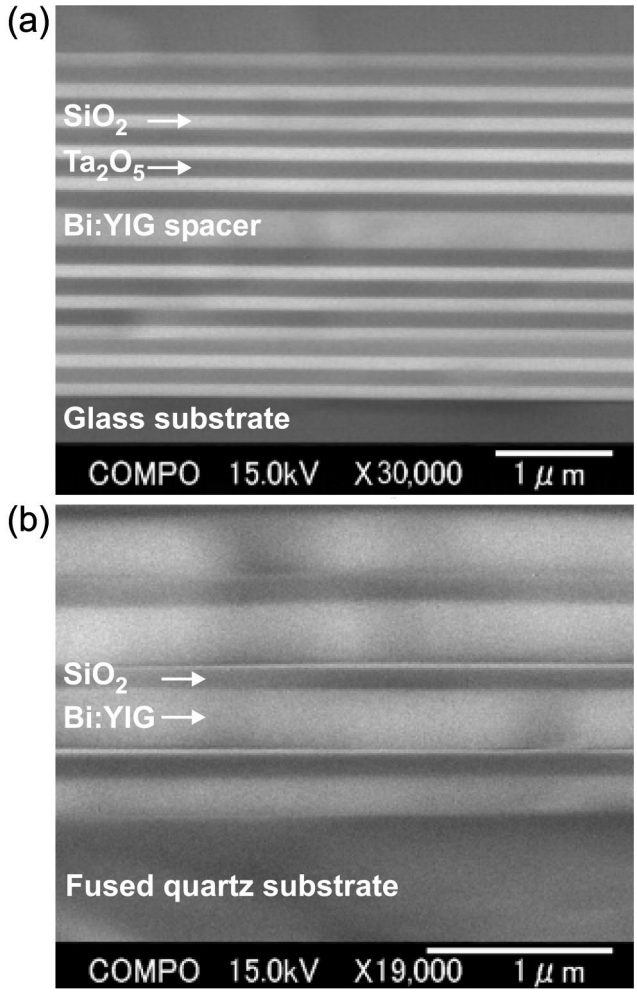

Fig. 1. FESEM images of the MMC (upper panel) and MPC (lower panel) cleavages.

rations of the nonlinear spectroscopy are used in the study. In the first one, the fundamental wavelength λ_ω is tuned at the fixed angle of incidence θ. This mode is termed below "spectroscopy in the frequency domain." The output of a nanosecond optical-parametric-oscillator laser system tunable from 720 nm to 1000 nm is used as the fundamental radiation. Laser energy is approximately 10 mJ per pulse, pulse width is below 2 ns, and laser spot area is 0.5 mm^2.

The case of tuning the angle of incidence while keeping the fundamental wavelength fixed is called angular spectroscopy or "spectroscopy in the wave-vector domain." For this the 1064-nm output of a nanosecond, YAG laser is used. Energy is below 10 mJ per pulse, pulse width is approximately 15 ns, and the laser spot area is 1.0 mm^2. Radiation at the SH or the TH wavelength is selected by an appropriate set of color and interference filters and detected by a photomultiplier tube. The SH-intensity spectrum acquired in the frequency domain is normalized over the spectral sensitivity of the detection system and tuning curve of the optical parametric oscillator by means of a SH-intensity reference channel operating with a slightly wedged, *z*-cut quartz plate and with the detection system identical to that in the sample channel.

The saturating dc magnetic field of strength up to 2 kOe that provides the single-domain state is applied tangentially to the samples for the longitudinal and transversal NOMOKE, or along the normal to the samples for the polar NOMOKE with a permanent FeNdB magnet.

4. RESULTS AND DISCUSSION

A. Optical and Magneto-Optical Spectra of Magnetophotonic Crystals and Microcavities

Figure 2 shows the transmission spectrum of a MMC. Low transmission is observed in the spectral region from 750 nm to 1000 nm where transmittance is decreased down to 10^{-3}. This corresponds to the PBG of the microcavity. The PBG spectral width and the value of attenuation in the PBG are determined by the number of repetitions and the refractive-index difference in the SiO_2–Ta_2O_5 Bragg reflectors. A peak in the transmittance spectrum observed at 910 nm is attributed to the microcavity mode. The quality factor of the MMC is $Q_\omega = \lambda_0/\Delta\lambda_0 \approx 75$, where λ_0 is the resonant wavelength and $\Delta\lambda_0$ is FWHM. The spectrum of the Faraday rotation angle θ_F measured by crossed Glan-prism polarizer and analyzer is also shown in Fig. 2. The θ_F spectrum has a peak at the MMC mode where θ_F is enhanced up to $-1.5°$. This corresponds to an effective rotation value of $-7.7°/\mu m$, which is ≈50 times larger than the Faraday rotation in a single Bi:YIG film on the same substrate measured at this wavelength.

The optical transmission spectrum of a MPC is shown in Fig. 3. The spectral region from 850 nm to 1100 nm with a small transmittance indicates the PBG. The smallest transmittance value is reached at $\lambda_\omega \approx 965$ nm and is approximately 0.10. Outside the PBG, the optical spectrum shows interference fringes, where transmittance is increased up to 0.9. θ_F is enhanced up to $-0.8°$ at the long-wavelength edge of the PBG at 1100 nm. This corresponds to an effective value of $-0.75°/\mu m$, which is approximately 8 times larger than the Faraday rotation in the single Bi:YIG film at this wavelength. For the wavelengths tuned inside the PBG, Faraday rotation is strongly suppressed. Peaks of θ_F at 750 nm and

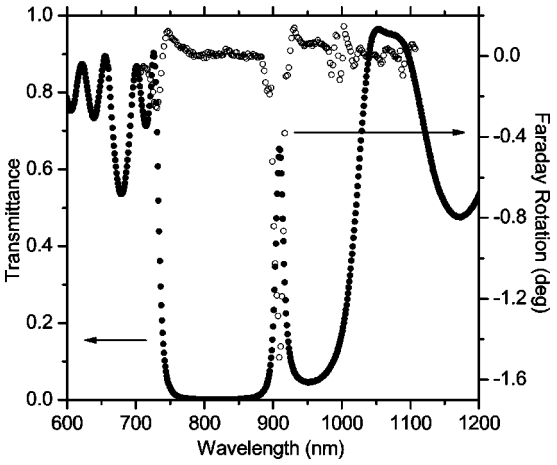

Fig. 2. Spectra of transmittance (filled circles) and the Faraday rotation angle (open circles) of the MMC with $\lambda_{MC} \approx 900$ nm measured at normal incidence.

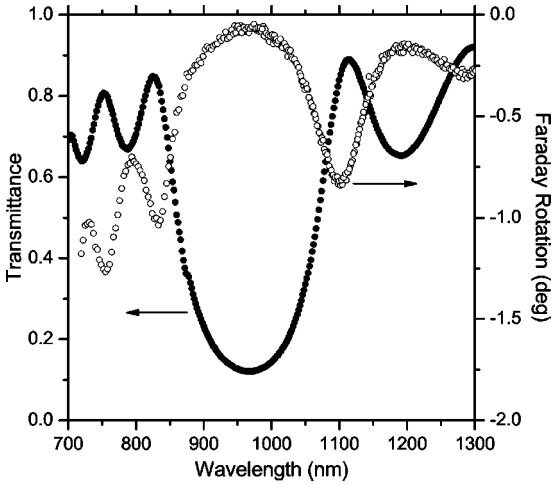

Fig. 3. Spectra of transmittance (filled circles) and the Faraday rotation angle (open circles) of the MPC with $\lambda_{PC} \approx 950$ nm measured at normal incidence.

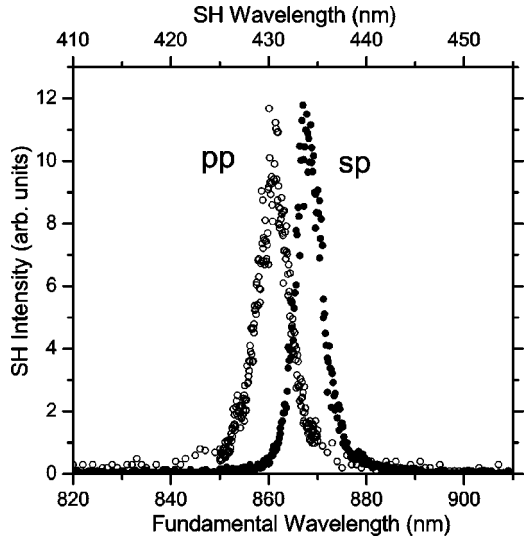

Fig. 4. SHG spectra of the MMC with $\lambda_{MC} \approx 900$ nm measured in the *p*-in, *p*-out (open circles) and *s*-in, *p*-out (filled circles) polarization combinations.

830 nm correlate with transmission spectrum maxima. The θ_F increase with the decrease in wavelength associated with the Faraday rotation spectrum of Bi:YIG.

B. Resonant Second- and Third-Harmonic Generation in Magnetophotonic Microcavities

The SHG spectra of MMC are presented in Fig. 4. The spectra have peaks in the fundamental wavelength interval from 850 nm to 880 nm. For oblique angles of incidence, the modes are shifted to the shorter fundamental wavelength and observed at $\lambda_\omega = \lambda_{MC}(1 - n_{YIG}^{-2} \sin^2 \theta)^{1/2}$, where n_{YIG} is the refractive index of the Bi:YIG spacer. The peak positions correlate with the microcavity modes for the *s*- and *p*-polarized fundamental radiation and are separated by 10 nm. The SH intensity $I_{2\omega}$ at the microcavity mode is enhanced by a factor of at least 10^3 relative to that outside the PBG, where fundamental wave propagation is allowed. The quality factor of the SHG resonances $Q_{2\omega} \approx 160 \pm 5$, which is approximately twice as large as Q_ω. The SH intensity is negligible at the PBG edge of the MMC, where phase-matched SHG from layers forming mirrors is expected.[5,7] Thus the SiO_2–Ta_2O_5 Bragg reflectors are considered linear media. The SHG enhancement is due to the spatial localization of the resonant fundamental radiation in the spacer. The negligible SHG signal observed in the *s*-in, *s*-out and *p*-in, *s*-out polarization combinations confirms the symmetry considerations for nonzero elements of the $\chi^{(2,0)}$ and $\chi^{(2,1)}$ tensors.

Similar resonant enhancement produced by fundamental radiation localization is observed in THG. Figure 5 shows the angular THG spectra measured in the *p*-in, *p*-out and *s*-in, *s*-out polarization combinations. These polarization combinations are the only ones allowed in the case of nonmagnetic THG in the in-plane isotropic films. The angular spectra have the peaks of the TH intensity $I_{3\omega}$ at the angle of incidence corresponding to the resonance of the fundamental radiation with the microcavity mode. As in the case of the SHG, *p*- and *s*-polarized modes are shifted by 1.5°–2° relative to each other.

The spectral splitting of the SHG peaks for *s*- and *p*-polarized fundamental waves is associated with the splitting of the microcavity modes for these polarization states that is most likely a manifestation of the strain-induced anisotropy of the Bi:YIG layer and of the nonequal diagonal elements of the permittivity tensor. Birefringence in the Bi-substituted iron garnet films with optical axis along the film normal[42] is attributed to a mismatch in the film and substrate lattice parameters as well as to the lattice distortions from the Fe ions on the octahedral and tetrahedral sites.[43] In polycrystalline garnet films prepared on quartz substrates, uniaxial optical anisotropy accompanied by magnetic anisotropy can also be induced by garnet lattice distortions due to O vacancies

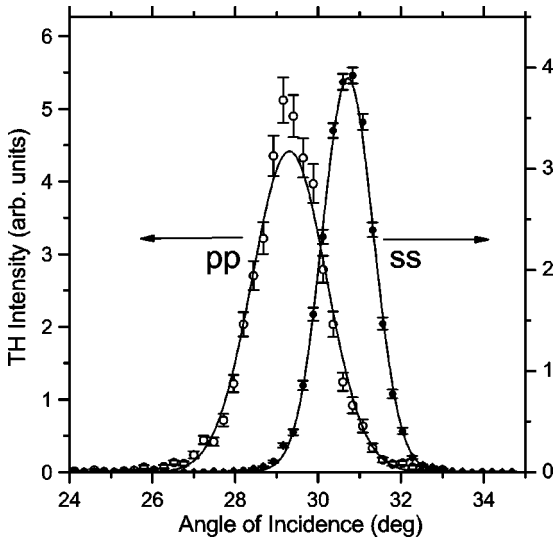

Fig. 5. THG spectra of the MMC with $\lambda_{MC} \approx 1115$ nm measured in the *p*-in, *p*-out (open circles) and *s*-in, *s*-out (filled circles) polarization combinations.

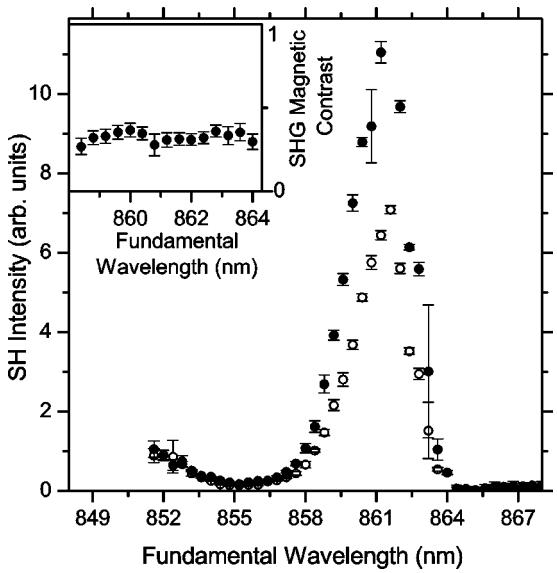

Fig. 6. Intensity effects in MSHG: the spectrum of transversal NOMOKE in SHG measured in the *p*-in, *p*-out polarization combination for opposite directions of magnetization. Filled circles stand for M_Y and open circles for $-M_Y$. Inset: spectral dependence of the SHG magnetic contrast when the fundamental wavelength is in the vicinity of the microcavity mode.

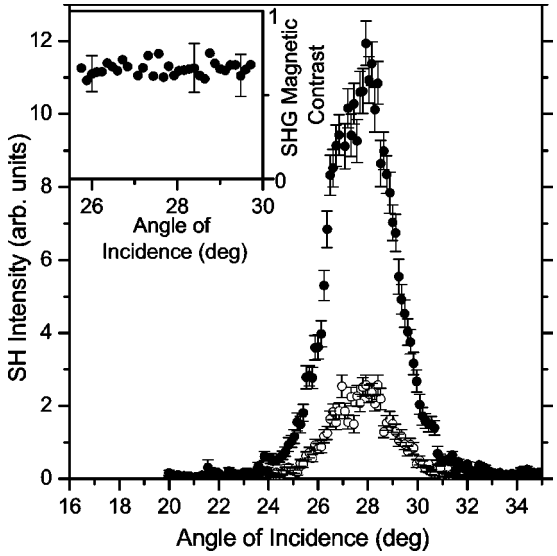

Fig. 7. Intensity effects in MSHG: the angular dependence of transversal NOMOKE in SHG measured in the *p*-in, *p*-out polarization combination for opposite directions of magnetization. Filled circles stand for M_Y and open circles for $-M_Y$. Inset: the angular spectrum of the SHG magnetic contrast when the fundamental angle of incidence is in the vicinity of the microcavity mode.

and to the difference in thermal expansion coefficients of the film and the substrate.[37]

C. MSHG in Magnetophotonic Microcavities

1. Transversal NOMOKE in MSHG: Intensity and Phase Effects

Figure 6 shows SH intensity as a function of the fundamental wavelength measured in the MMC with $\lambda_{MC} \approx 900$ nm for opposite directions of the dc magnetic field applied in the transversal configuration $\mathbf{M} = (0, M_Y, 0)$.[34] The SH intensity is enhanced as the fundamental wave is tuned across the microcavity mode. The ratio of the intensities for opposite directions of the magnetic field is almost 2. Spectral dependence of the magnetic contrast in the SH intensity $\rho = (I_+ - I_-)/(I_+ + I_-)$, where + and − denote directions of the field, is shown in the inset of Fig. 6. ρ achieves values of 0.3 and appears to be independent of the wavelength. Inverting the magnetic field direction varies only the SH intensity, and no spectral shifts of SHG resonances are observed.

Figure 7 shows the SH intensity as a function of the angle of incidence measured in the MMC with $\lambda_{MC} \approx 1115$ nm in the transversal NOMOKE configuration. Inverting the magnetic field direction varies $I_{2\omega}$ by a factor of ≈4. The angular spectrum of the SHG magnetic contrast shown in the inset of Fig. 7 is independent of the angle of incidence and achieves values of 0.65.

Magnetization-induced changes of the relative phase of the SH wave are observed through SHG interferometry.[44] The SHG interference patterns are obtained by translation along the laser beam of the SHG reference sample, thus varying the distance l between the reference and the MMC sample. The SHG reference sample is a 30-nm-thick $InSnO_x$ oxide film deposited on a fused quartz plate. The total SH intensity $I_{2\omega}(l, \mathbf{M})$ is produced by the coherent sum of the SH waves from the reference $\mathbf{E}^r_{2\omega}$ and the MMC sample $\mathbf{E}_{2\omega}(\mathbf{M})$:

$$I_{2\omega}(l, \mathbf{M}) = \frac{c}{8\pi}|\mathbf{E}^r_{2\omega}(l) + \mathbf{E}_{2\omega}(\mathbf{M})|^2$$
$$= I^r_{2\omega} + I_{2\omega}(\mathbf{M}) + 2\alpha[I^r_{2\omega} I_{2\omega}(\mathbf{M})]^{1/2} \times \cos[2\pi kl + \Phi_{rs}(\mathbf{M})], \quad (5)$$

where $k = 2\Delta n/\lambda_\omega$ with $\Delta n = n_{2\omega} - n_\omega$ describing air dispersion, Φ_{rs} is the phase difference between the reference and sample SH waves, and $\alpha < 1$ is the phenomenological parameter accounting for both spatial and temporal coherence of the laser pulses. Changing the magnetic

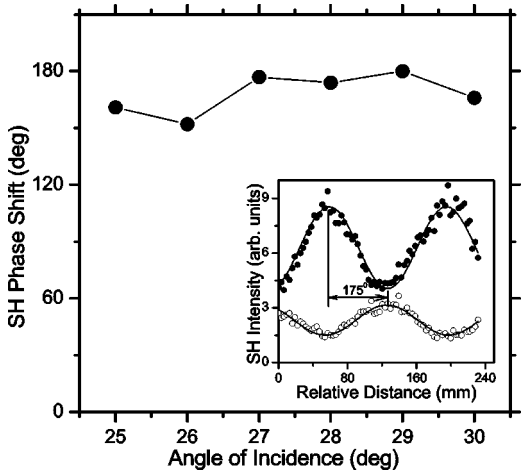

Fig. 8. Phase effects in MSHG: magnetization-induced shift of the relative SH phase measured in the transversal NOMOKE configuration in the angular vicinity of the microcavity mode. Inset: row SHG interference patterns for opposite directions of the magnetic field measured at $\theta = 28°$.

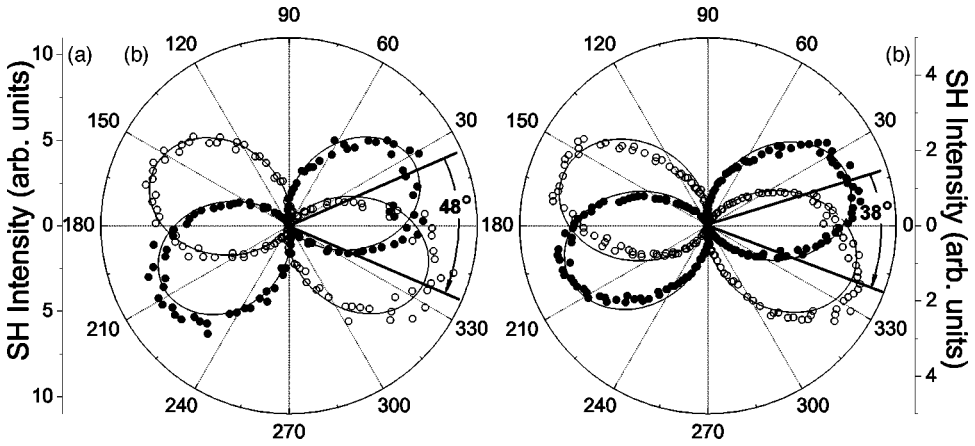

Fig. 9. SH-wave polarization diagrams measured for opposite directions of magnetic field applied in the longitudinal configuration to the MMC with $\lambda_{MC} \approx 900$ nm. The angle of incidence is (a) 15° or (b) 30°. The zeroth value of the analyzer angle corresponds to the *p*-polarized SH wave. Curves are the fit to intensity of the linearly polarized wave.

field direction to the opposite one shifts the SHG interference patterns by almost half a period. This indicates the shift of the relative SH phase at ≈180°. The angular dependence of the SH phase shifts measured at the vicinity of the mode is shown in Fig. 8. The phase shifts are slightly smaller than 180° and almost constant in θ.

The SH intensity variations that are odd in the magnetization are observed only in the transversal NOMOKE configuration. In the *p*-in, *p*-out polarization combination, the nonmagnetic (crystallographic) SH field E^{NM} is induced by the χ_{zzz}, χ_{zxx}, and χ_{xxz} elements of the $\chi^{(2,0)}$ tensor. The magnetization-induced SH field $E^{M}\exp(i\varphi_M)$ is generated by the χ_{xzzY}, χ_{zxzY}, and χ_{xxxY} elements of the $\chi^{(2,1)}$ tensor and is shifted in phase by φ_M with respect to the E^{NM} field. Interference of the nonmagnetic and magnetization-induced SH fields leads to the cross term $\pm 2E^{NM}E^{M}\cos\varphi_M$ in the SH intensity. This term changes sign upon reversal of the magnetic field direction and results in the SH intensity variations, which are linear in **M**. The relative value of these variations depends on the phase shift φ_M. The constant value of ρ in the vicinity of the microcavity mode indicates that the SH fields E^{NM} and E^{M} are enhanced similarly as a result of fundamental field localization. For the 1064-nm fundamental wavelength, φ_M takes values close to 0° or to 180° for opposite directions of **M**. This is seen in phase measurements, where the magnetization-induced shift of the relative SH phase is close to 180°. For small refraction angle θ_ω in the Bi:YIG layer and $\varphi_M \approx 0$, the ratio between E^{NM} and E^{M} can be estimated as

$$E^{NM}/E^{M} \approx \chi_{xxxY}M_Y/(2\chi_{zxx}\tan\theta_\omega). \qquad (6)$$

This gives the ratio of $\chi_{xxxY}M_Y/\chi_{zxx} \approx 0.15$ for $\rho \approx 0.65$.

2. *Longitudinal and Polar NOMOKE in MSHG: Polarization Effects*

Figure 9 shows dependences of the SH intensity on the orientation angle Θ of the analyzer axis measured for opposite directions of magnetic field applied in the longitudinal NOMOKE configuration.[35] The fundamental radiation is *s* polarized and its wavelength is 868 nm, which corresponds to the microcavity mode. The SH wave is strongly linearly polarized. The longitudinal NOMOKE

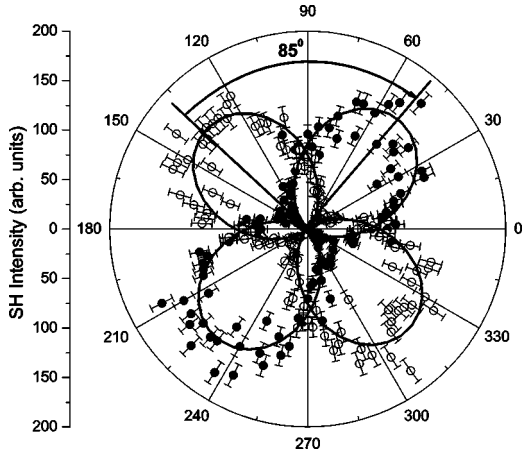

Fig. 10. SH-wave polarization diagrams measured for opposite directions of magnetic field applied in the longitudinal configuration to the MMC with $\lambda_{MC} \approx 1115$ nm. The angle of incidence is 28°. The zeroth value of the analyzer angle corresponds to the *p*-polarized SH wave. Curves are the fit to intensity of the linearly polarized wave.

manifests itself in the magnetization-induced rotation of the SH wave polarization. The angle of polarization rotation is $\Delta\Theta = 38°$ for angle of incidence of 30° and almost $\Delta\Theta = 48°$ for 15° incidence.

The magnetization-induced rotation of the SH wave polarization plane is increased as the fundamental radiation is tuned to the long-wavelength region. Figure 10 shows the SH-wave polarization diagrams measured for the *s*-polarized fundamental radiation with $\lambda_\omega = 1064$ nm. Magnetization-induced rotation of the polarization plane up to $\Delta\Theta = 85°$ is observed, while for the *p*-polarized fundamental radiation the ΔΘ value is ≈60°.

In the longitudinal NOMOKE configuration, the nonmagnetic and magnetization-induced SH fields are polarized orthogonally, E^{NM} being *p*-polarized and E^{M}, *s*-polarized, respectively. The magnetization-induced effects appear in rotation of the polarization plane of the total SH light. The SH intensity depends on the analyzer angle Θ as

$$I_{2\omega}(\Theta) \propto |E_p^{NM}\cos\Theta + E_s^{M}\exp(i\phi_M)\sin\Theta|^2, \qquad (7)$$

where the phase shift ϕ_M describes the SH-field ellipticity, and subscripts s and p indicate the polarization of corresponding SH fields. The SH wave is considered as linearly polarized with $\phi_M \approx 0$. The rotation angle of the SH-field polarization on reversal of the magnetic field direction is estimated as $\Delta\Theta \approx 2\arctan(E_s^M/E_p^{NM})$ and depends on the ratio of corresponding elements of the $\chi^{(2,0)}$ and $\chi^{(2,1)}$ tensors.[35] For the longitudinal NOMOKE configuration and the s-polarized fundamental radiation

$$\Delta\Theta \approx 2\arctan[\chi_{yyyX}M_X/\chi_{zyy}\sin\theta_\omega]. \quad (8)$$

For $\Delta\Theta_{2\omega} = 48°$ and $\theta = 15°$ this gives the ratio $\chi_{yyyX}M_X/\chi_{zyy} \approx 0.1$ at $\lambda_\omega = 870$ nm, which is close to the value of the $\chi_{xxxY}M_Y/\chi_{zxx}$ ratio estimated in transversal NOMOKE. For $\Delta\Theta_{2\omega} = 85°$, $\theta = 28°$, it gives the ratio $\chi_{yyyX}M_X/\chi_{zyy} \approx 0.15$ at $\lambda_\omega = 1064$ nm.

The spectrum of the polar NOMOKE is shown in Fig. 11. Tuning the fundamental wavelength through the microcavity mode leads to a gradual increase of $\Delta\Theta$ from 1° to 7°. In the polar NOMOKE configuration, E_s^M is yielded by three sources. First is generation of the s-polarized, magnetization-induced SH field by the χ_{yxzZ} element $E_{s,1}^M = F_y^{2\omega}F_x^\omega F_z^\omega \chi_{yxzZ}M_Z I_\omega{}^2$, with F_i^Ω as the Green's-function correction for the corresponding component of the SH- or fundamental-wave amplitudes[45] and I_ω as the fundamental-wave intensity. The second source is the generation of the s-polarized SH field through the χ_{yzy} element of the crystallographic quadratic susceptibility $E_{s,2}^M = F_y^{2\omega}F_z^\omega F_y^\omega \chi_{yzy} I_\omega{}^2 \sin(\Theta_\omega/2)$, where Θ_ω is the linear (Faraday) rotation angle of the fundamental wave. The Faraday rotation of the fundamental radiation is greatly enhanced at the resonance with the microcavity mode as a result of multiple reflection in the Bi:YIG spacer[30] that is directly attributed to the nonreciprocity of the light propagation in the magnetic materials. Faraday rotation of the initially p-polarized fundamental wave is equivalent to the appearance of the s-polarized component of the fundamental radiation that allows generation of the s-polarized SH wave in the m-in, s-out polarization combination. The third source of the s-polarized SH wave is the Faraday rotation of the p-polarized SH wave $E_{s,3}^M = E_p^{NM}\sin(\Theta_{2\omega}/2)$, where $\Theta_{2\omega}$ is the Faraday rotation angle of the SH wave. For small angles of incidence the contribution of the χ_{zzz} susceptibility element is small and $E_p^{NM} = [F_z^{2\omega}(F_x^\omega)^2\chi_{zxx} + F_x^{2\omega}F_z^\omega F_x^\omega \chi_{xzx}]I_\omega{}^2$. For the correct calculation of the total SH-wave polarization rotation $\tan\Delta\Theta = 2(E_{s,1}^M + E_{s,2}^M + E_{s,3}^M)/E_p^{NM}$, one should know the relation between the χ_{yzy}, χ_{zxx}, and χ_{xzx} elements. However, for our estimation, we assume them to be equal. For small refractive angles θ_ω, Green's-function corrections $F_z^{2\omega}$, $F_z^\omega \to 0$ and $F_x^{2\omega}$, F_x^ω, F_y^ω, $F_y^{2\omega} \to 1$, $\tan\Delta\Theta \approx \Delta\Theta$, $\sin\Theta_{2\omega} \approx \Theta_{2\omega}$, and $\sin\Theta_\omega \approx \Theta_\omega$. The $\Delta\Theta$ value can be estimated with these assumptions as[25]

$$\Delta\Theta \approx \chi_{yxzZ}M_Z/\chi_{zxx} + \Theta_\omega/2 + \Theta_{2\omega}. \quad (9)$$

The first term on the right-hand side of Eq. (9) is wavelength-independent since the elements of the $\chi^{(2,0)}$ and $\chi^{(2,1)}$ tensors are constant within the narrow spectral region of the MC mode. The term $\Theta_{2\omega}$ is also independent of λ_ω because of large absorption at the SH wavelength. The second term $\Theta/2$ as a function of λ_ω and reaches a maximum for oblique angles of incidence when the s and p modes are overlapped. Note that the rotation of the SH field polarization plane through *nonmagnetic* quadratic susceptibility relates strongly to the symmetry of the magnetic spacer since it requires a nonzero χ_{yzy} element.

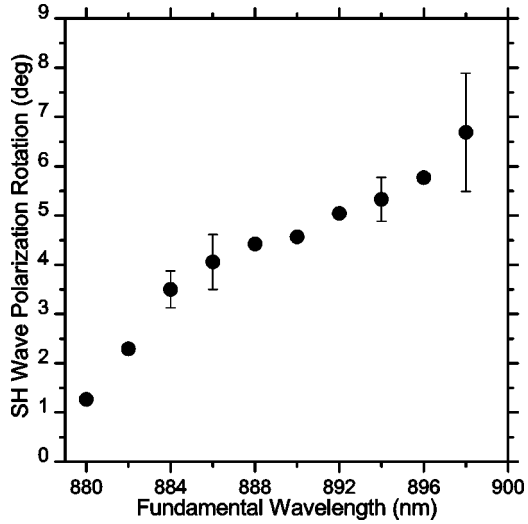

Fig. 11. Polarization effects in MSHG: spectrum of the SH-wave polarization rotation in MMC with $\lambda_{MC} \approx 900$ nm on inversion of the magnetic field direction in the polar NOMOKE configuration.

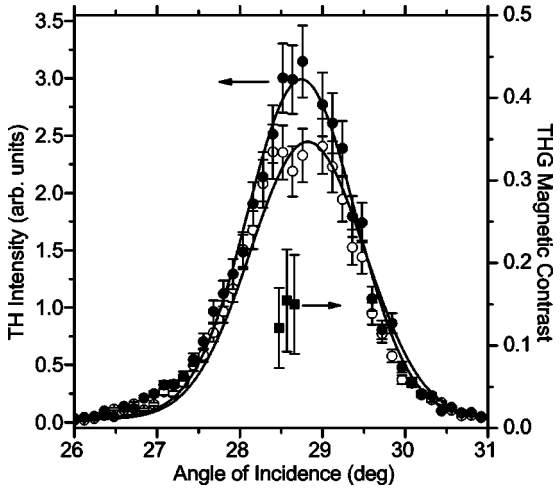

Fig. 12. Intensity effects in MTHG: angular spectra of transversal NOMOKE in THG measured in MMC with $\lambda_{MC} \approx 1115$ nm for opposite directions of magnetization. Filled circles stand for M_Y and open circles for $-M_Y$. Squares show the THG magnetic contrast in the angular vicinity of the microcavity mode.

D. MTHG in Magnetophotonic Microcavities

Magnetization-induced effects on the intensity of THG were studied for the transversal NOMOKE configuration. A symmetry analysis shows that for this geometry of the magnetic field application, elements of the cubic susceptibility tensor $\chi^{(3,1)}$, which are odd in the magnetization, lead to the appearance of additional contributions to the p-polarized THG signal. The experiments performed for the p-in, p-out polarization combination in the transver-

sal NOMOKE do not reveal magnetization-induced variations of the THG intensity within the experimental accuracy, in contrast to a large magnetic variation in the SH intensity. To reveal a small magnetization-induced effect in the THG intensity, the following experimental scheme is chosen. The *p*-polarized THG intensity is measured while the polarization plane of the fundamental radiation is chosen to form an angle of 5–10° from the *s* polarization. For this polarization combination almost the entire magnetic component of the THG intensity generated by the χ_{zyyyX} component is recorded that has interfered with a strongly suppressed, nonmagnetic *p*-in, *p*-out THG signal. Figure 12 shows the THG spectra measured in the wave-vector domain for the oppositely directed magnetic field in the transversal NOMOKE configuration. As in the magnetization-induced SHG, the THG magnetic contrast is determined by the expression $\rho_{3\omega} = (I_+^{3\omega} - I_-^{3\omega})/(I_+^{3\omega} + I_-^{3\omega})$, where $I_+^{3\omega}$ and $I_-^{3\omega}$ are the THG intensities for the oppositely directed magnetic fields. The measured value of the magnetic contrast in the THG intensity is found to be ≈0.1 for the angles of incidence corresponding to the resonance with the microcavity mode.

The observed THG magnetic contrast is due to the THG by the $\chi^{(3,1)}$ components and their interference with the nonmagnetic components due to the internal homodyne effect. This results in the revelation of a weak magnetic THG contribution against the background of a much stronger nonmagnetic THG. In this case, an estimate can be made for the χ_{zyyyX} element as $\chi_{zyyyX} \approx 10^{-3}\chi_{\text{eff}}^{(3)}$, where $\chi_{\text{eff}}^{(3)}$ is the effective nonmagnetic cubic susceptibility responsible for the generation of the *p*-polarized TH field with *s*- or mixed-polarized fundamental radiation.

E. Phase-Matched MSHG in Magnetophotonic Crystals

Figure 13 shows the spectrum of the SH intensity measured in MPC for the *p*-in, *s*-out polarization combination in the longitudinal NOMOKE configuration. The spectrum demonstrates the resonance enhancement at $\lambda_\omega \approx 1055$ nm. The spectral position of the peak correlates with the long-wavelength PBG edge, which is blueshifted from 1110 nm for oblique angles of incidence. In the *p*-in, *s*-out polarization combination the nonmagnetic (crystallographic) SH field $E_{2\omega}^{\text{NM}}$ induced by the $\chi^{(2,0)}$ tensor is zero. Thus in longitudinal NOMOKE configuration as $\mathbf{M} = (M_X, 0, 0)$, the SH intensity is entirely associated with the magnetization-induced SH field $E_{2\omega}^{\text{M}}$ induced by the χ_{yxxX} and χ_{yzzX} elements of the $\chi^{(2,1)}$ tensor. The MSHG enhancement in MPCs is interpreted as the result of phase matching achieved when the fundamental wavelength is tuned across the PBG edge. This stems from comparison of amplitudes of the SHG resonances at PBG edges. The intensity enhancement at the long-wavelength PBG edge of a MPC is at least five times larger than that at the short-wavelength edge. Spatial localization of the optical field is similar at both PBG edges, and the SHG enhancement yielded by this mechanism is expected to be the same order of magnitude. Inverting the magnetic field direction does not change the value of the SH intensity, indicating that $E_{2\omega}^{\text{NM}} = 0$. This is in contrast to the *p*-in, *p*-out polarization combination. In the transversal NOMOKE configuration the nonmagnetic SH field $E_{2\omega}^{\text{NM}}$ interferes with the magnetization-induced SH field $E_{2\omega}^{\text{M}} \exp(i\varphi_M)$. The intensity cross term $\pm 2E_{2\omega}^{\text{NM}}E_{2\omega}^{\text{M}} \cos\varphi_M$ changes sign on changing the magnetic field direction and manifests the internal homodyne effect in MSHG. This term leads to variations of the SH intensity that are linear in $\mathbf{M}$ and depend on the relative phase φ_{M} between $E_{2\omega}^{\text{NM}}$ and $E_{2\omega}^{\text{M}}$. Figure 14 shows the SHG spectra measured for opposite directions of the magnetic field in the transversal NOMOKE configuration. The SH intensity is enhanced manyfold in the vicinity of 1050 nm corresponding to the phase-matched conditions for SHG at the long-wavelength PBG edge of the MPC. Changing the magnetic field direction varies the SH intensity approximately by a factor of seven at $\lambda_\omega \approx 1055$ nm, which indicates the noticeable interference between the $E_{2\omega}^{\text{NM}}$ and $E_{2\omega}^{\text{M}}$ fields. At $\lambda_\omega \approx 1025$ nm the SH intensity for one of the magnetic field directions is close to zero. This means that the contrast of the magnetization-induced variations in the SH intensity is close to unity, which is the upper limit for SHG magnetic contrast.

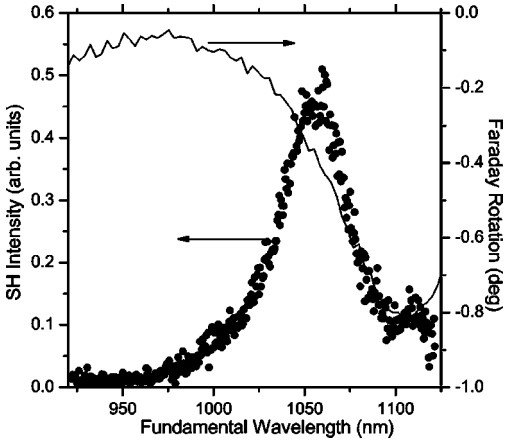

Fig. 13. Filled circles, intensity spectrum of the SH wave reflected from the MPC in the *p*-in, *s*-out polarization combination in longitudinal configuration of the dc-magnetic field application. Curve, the Faraday rotation spectrum at normal incidence.

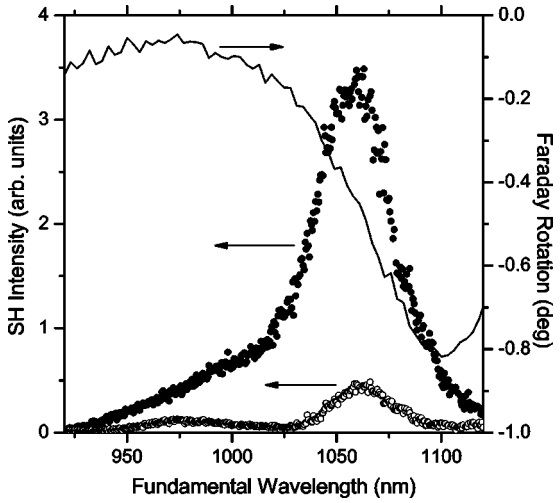

Fig. 14. SHG spectra of the MPC in the *p*-in, *p*-out polarization combination and in transversal magnetic field configuration measured for opposite directions of the dc-magnetic field, open and filled circles, respectively. Curve, the Faraday rotation spectrum at normal incidence.

5. CONCLUSIONS

In summary the nonlinear magneto-optical Kerr effect has been studied in magnetophotonic crystals and microcavities. Magnetization-induced second-harmonic generation was observed in MMCs with the spacer formed from Bi-substituted yttrium iron garnet. Localization of the fundamental radiation resonant with the microcavity mode in the garnet spacer enhances manyfold the absolute values of both nonmagnetic (crystallographic) SHG and MSHG in the MMCs. The transversal NOMOKE in SHG reveals itself in the magnetization-induced variation of the SH intensity with the magnetic contrast up to 0.65, and in the large close to 180° shift of the relative SH phase. The large, up to 85° magnetization-induced rotation of the SH-wave-polarization plane is observed for the longitudinal NOMOKE configuration. Multiple-reflection interference of the resonant fundamental radiation enhances additively the Faraday rotation of the fundamental-wave polarization. This results in enhancement of the SH-wave-polarization rotation in the polar configuration of the magnetic field.

Noticeable NOMOKE is observed in THG from MPCs. Magnetization-induced variations of the TH intensity with magnetic contrast up to 0.10 are observed in the transversal NOMOKE configuration.

MSHG reveals an intensity enhancement by a factor of more than 10^2 when the fundamental radiation is tuned across the PBG gap edge of MPCs consisting of stacks of magnetic garnet layers. The enhancement is a manifestation of the phase matching for MSHG fulfilled at the PBG edge of MPCs.

ACKNOWLEDGMENTS

The authors are pleased to acknowledge the assistance of R.V. Kapra in experiments, T. Yoshida and D. Kobayashi in sample fabrication, and A. V. Rassudov in tensorial calculations. This work is supported in part by the Russian Foundation for Basic Research (grants 04-02-16847 and 04-02-17059), the Presidential Grant for Leading Russian Science Schools (1604.2003.2), and grants-in-aid from the Ministry of Education, Science, Culture and Sport of Japan (14205045 and 14655119).

Corresponding author A. A. Fedyanin's e-mail address is fedyanin@shg.ru. O. A. Aktsipetrov's e-mail address is aktsip@shg.ru; his URL is http://www.shg.ru. M. Inoue's e-mail address is inoue_mitsuteru@eee.tut.ac.jp.

REFERENCES

1. K. Sakoda, *Optical Properties of Photonic Crystals* (Springer, Berlin, 2001).
2. M. Scalora, M. J. Bloemer, A. S. Manka, J. P. Dowling, C. M. Bowden, R. Viswanathan, and J. W. Haus, "Pulsed second-harmonic generation in nonlinear, one-dimensional, periodic structures," Phys. Rev. A **56**, 3166–3174 (1997).
3. N. Bloembergen and J. Sievers, "Nonlinear optical properties of periodic laminar structures," Appl. Phys. Lett. **17**, 483–485 (1970).
4. J. P. van der Ziel and M. Ilegems, "Optical second-harmonic generation in periodic multilayer GaAs-$Al_{0.3}Ga_{0.7}As$ structures," Appl. Phys. Lett. **28**, 437–439 (1976).
5. Y. Dumeige, P. Vidakovic, S. Sauvage, I. Sagnes, J. A. Levenson, C. Sibilia, M. Centini, G. D'Aguanno, and M. Scalora, "Enhancement of second-harmonic generation in a one-dimensional semiconductor photonic bandgap," Appl. Phys. Lett. **78**, 3021–3023 (2001).
6. A. V. Balakin, V. A. Bushuev, N. I. Koroteev, B. I. Mantsyzov, I. A. Ozheredov, A. P. Shkurinov, D. Boucher, and P. Masselin, "Enhancement of second-harmonic generation with femtosecond laser pulses near the photonic band edge for different polarizations of incident light," Opt. Lett. **24**, 793–795 (1999).
7. T. V. Dolgova, A. I. Maidykovski, M. G. Martemyanov, A. A. Fedyanin, O. A. Aktsipetrov, G. Marowsky, V. A. Yakovlev, and G. Mattei, "Giant microcavity enhancement of second-harmonic generation in all-silicon photonic crystals," Appl. Phys. Lett. **81**, 2725–2727 (2002).
8. J. Trull, R. Vilaseca, J. Martorell, and R. Corbalan, "Second-harmonic generation in local modes of a truncated periodic structure," Opt. Lett. **20**, 1746–1748 (1995).
9. H. Cao, D. Hall, J. Torkelson, and C.-Q. Cao, "Large enhancement of second-harmonic generation in polymer films by microcavities," Appl. Phys. Lett. **76**, 538–540 (2001).
10. S. Lettieri, S. D. Finizio, P. Maddalena, V. Ballarini, and F. Giorgis, "Second-harmonic generation in amorphous silicon nitride microcavities," Appl. Phys. Lett. **81**, 4706–4708 (2002).
11. T. V. Dolgova, A. I. Maidykovski, M. G. Martemyanov, A. A. Fedyanin, O. A. Aktsipetrov, D. Schuhmacher, G. Marowsky, V. A. Yakovlev, G. Mattei, N. Ohta, and S. Nakabayashi, "Giant optical second-harmonic generation in single and coupled microcavities on the base of one-dimensional photonic crystals," J. Opt. Soc. Am. B **19**, 2129–2140 (2002).
12. O. A. Aktsipetrov, O. V. Braginskii, and D. A. Esikov, "Nonlinear optics of gyrotropic media: second-harmonic generation in rare-earth iron garnets," Sov. J. Quantum Electron. **20**, 259–263 (1990).
13. O. A. Aktsipetrov, O. V. Braginskii, and D. A. Esikov, "Magnetization-induced second-harmonic generation in thin granular films," in *Proceedings of 13th International Conference on Coherent and Nonlinear Optics, ICONO-13*, Vol. 2 (Academkniga, Minsk, USSR, 1988), p. 142.
14. J. Reif, J. C. Zink, C.-M. Schneider, and J. Kirschner, "Effects of surface magnetism on optical second-harmonic generation," Phys. Rev. Lett. **67**, 2878–2881 (1991).
15. J. Reif, C. Rau, and E. Matthias, "Influence of magnetism on second-harmonic generation," Phys. Rev. Lett. **71**, 1931–1934 (1993).
16. G. Spierings, V. Koutsos, H. A. Wierenga, M. W. J. Prins, D. Abraham, and T. Rasing, "Optical second-harmonic generation study of interface magnetism," Surf. Sci. **287–288**, 747–749 (1993).
17. G. Spierings, V. Koutsos, H. A. Wierenga, M. W. J. Prins, D. Abraham, and T. Rasing, "Interface magnetism studied by optical second-harmonic generation," J. Magn. Magn. Mater. **121**, 109–111 (1993).
18. B. Koopmans, M. G. Koerkamp, and T. Rasing, "Observation of large Kerr angles in the nonlinear optical response from magnetic multilayers," Phys. Rev. Lett. **74**, 3692–3695 (1995).
19. A. Kirilyuk, T. Rasing, B. Doudin, and J.-P. Ansermet, "Nonlinear magneto-optical response of Co–Cu multilayered nanowires (abstract)," J. Appl. Phys. **81**, 4723 (1997).
20. V. V. Pavlov, R. V. Pisarev, A. Kirilyuk, and T. Rasing, "Observation of a transversal nonlinear magneto-optical effect in thin magnetic garnet films," Phys. Rev. Lett. **78**, 2004–2007 (1997).
21. O. A. Aktsipetrov, V. A. Aleshkevich, A. V. Melnikov, T. V. Misuryaev, T. V. Murzina, and V. V. Randoshkin, "Magnetic field induced effects in optical second-harmonic generation from iron-garnet films," J. Magn. Magn. Mater. **165**, 421–423 (1997).
22. V. N. Gridnev, V. V. Pavlov, R. V. Pisarev, A. Kirilyuk, and T. Rasing, "Second-harmonic generation in anisotropic magnetic films," Phys. Rev. B **63**, 184407–184417 (2001).
23. T. V. Murzina, E. Ganshina, V. S. Guschin, T. V. Misuryaev, and O. A. Aktsipetrov, "Nonlinear magneto-optical Kerr effect and second-harmonic generation interferometry in

Co–Cu granular films," Appl. Phys. Lett. **73**, 3769–3771 (1998).
24. T. V. Murzina, T. V. Misuryaev, A. F. Kravets, J. Güdde, D. Schuhmacher, G. Marowsky, A. A. Nikulin, and O. A. Aktsipetrov, "Nonlinear magneto-optical Kerr effect and plasmon assisted SHG in magnetic nanomaterials exhibiting giant magnetoresistance," Surf. Sci. **482–485**, 1101–1106 (2001).
25. A. A. Fedyanin, T. Yoshida, K. Nishimura, G. Marowsky, M. Inoue, and O. A. Aktsipetrov, "Magnetization-induced second-harmonic generation in magnetophotonic microcavities based on ferrite garnets," JETP Lett. **76**, 527–531 (2002).
26. A. A. Fedyanin, T. Yoshida, K. Nishimura, G. Marowsky, M. Inoue, and O. A. Aktsipetrov, "Nonlinear magneto-optical Kerr effect in gyrotropic photonic bandgap structures: magneto-photonic microcavities," J. Magn. Magn. Mater. **258–259**, 96–98 (2003).
27. T. V. Murzina, R. V. Kapra, A. A. Rassudov, O. A. Aktsipetrov, K. Nishimura, H. Uchida, and M. Inoue, "Magnetization-induced third-harmonic generation in magnetophotonic microcavities," JETP Lett. **77**, 537–540 (2003).
28. S. V. Lazarenko, A. Kirilyuk, T. Rasing, and J. C. Lodder, "Linear and nonlinear magneto-optical diffraction from one-dimensional periodic structures," J. Appl. Phys. **93**, 7903–7905 (2003).
29. I. L. Lyubchanskii, N. N. Dadoenkova, M. I. Lyubchanskii, E. A. Shapovalov, and T. Rasing, "Magnetic photonic crystals," J. Phys. D **36**, R277–R287 (2003).
30. M. Inoue, K. Arai, T. Fujii, and M. Abe, "One-dimensional magneto-photonic crystals," J. Appl. Phys. **85**, 5768–5770 (1999).
31. E. Takeda, N. Todoroki, Y. Kitamoto, M. Abe, M. Inoue, T. Fujii, and K. Arai, "Faraday effect enhancement in Co–ferrite layer incorporated into one-dimensional photonic crystal working as a Fabry-Perot resonator," J. Appl. Phys. **87**, 6782–6784 (2000).
32. T. Yoshida, K. Nishimura, H. Uchida, and M. Inoue, "One-dimensional magnetophotonic crystals with granular magnetic films," J. Appl. Phys. **93**, 6942–6944 (2003).
33. A. A. Fedyanin, O. A. Aktsipetrov, D. Kobayashi, K. Nishimura, H. Uchida, and M. Inoue, "Enhanced Faraday and nonlinear magneto-optical Kerr effects in magnetophotonic crystals," J. Magn. Magn. Mater. **282**, 256–259 (2004).
34. T. Murzina, T. Dolgova, R. Kapra, A. Fedyanin, O. Aktsipetrov, K. Nishimura, H. Uchida, and M. Inoue, "Magnetization-induced second-harmonic generation in magnetophotonic crystals," Phys. Rev. B **70**, 12407–12410 (2004).
35. T. Dolgova, A. Fedyanin, O. A. Aktsipetrov, K. Nishimura, H. Uchida, and M. Inoue, "Nonlinear magneto-optical Kerreffect in garnet magnetophotonic crystals," J. Appl. Phys. **95**, 7330–7332 (2004).
36. B. B. Krichevtsov, V. V. Pavlov, and R. V. Pisarev, "Giant linear magnetoelectric effect in garnet ferrite films," JETP Lett. **49**, 535–539 (1989).
37. E. Popova, N. Keller, F. Gendron, M. Guyot, M.-C. Brianso, Y. Dumond, and M. Tessier, "Structure and magnetic properties of yttrium iron garnet thin films prepared by laser deposition," J. Appl. Phys. **90**, 1422–1428 (2001).
38. G. Petrocelli, S. Martellucci, and M. Richetta, "Bismuth-induced enhancement of the second-harmonic generation efficiency in bismuth-substituted yttrium iron garnet films," Appl. Phys. Lett. **63**, 3402–3404 (1993).
39. R. V. Pisarev, B. B. Krichevtsov, V. N. Gridnev, V. P. Klin, D. Frohlich, and C. Pahlke-Lerche, "Opical second-harmonic generation in magnetic garnet thin films," J. Phys. Condens. Matter **5**, 8621–8628 (1993).
40. I. L. Lyubchanskii, N. N. Dadoenkova, M. I. Lyubchanskii, T. Rasing, J.-W. Jeong, and S.-C. Shinb, "Second-harmonic generation from realistic film–substrate interfaces: the effects of strain," Appl. Phys. Lett. **76**, 1848–1850 (2000).
41. S. Wittekoek, T. J. A. Popma, J. M. Robertson, and P. F. Bongers, "Magneto-optic spectra and the dielectric tensor elements of bismuth-substituted iron garnets at photon energies between 2.2–5.2 eV," Phys. Rev. B **12**, 2777–2788 (1975).
42. A. S. Trifonov, A. N. Ageev, V. N. Gridnev, O. G. Rutkin, V. B. Kravchenko, and L. M. Filimonova, "Optical anisotropy of iron garnet films containing bismuth," Sov. Phys. Tech. Phys. **30**, 1173–1176 (1985).
43. H. Lenz, P. Hansen, and W. Tolksdorf, "Growth-induced magnetic and optic anisotropy in bismuth-substituted iron garnet films," Appl. Phys. Lett. **54**, 2484–2486 (1989).
44. K. Kemnitz, K. Bhattacharyya, J. Hicks, G. Pinto, K. Eisenthal, and T. Heinz, "The phase of second-harmonic light generated at an interface and its relation to absolute molecular orientation," Chem. Phys. Lett. **131**, 285–288 (1986).
45. P. Guyot-Sionnest, W. Chen, and Y. R. Shen, "General considerations on optical second-harmonic generation from surfaces and interfaces," Phys. Rev. B **33**, 8254–8263 (1986).